Earth Planet. Sci. Lett. 684 (2026) 120004

Contents lists available at ScienceDirect

Earth and Planetary Science Letters

journal homepage: www.elsevier.com/locate/epsl

New insights into plateau-craton interactions from P and S wave tomography beneath the northeastern Tibetan plateau

Haibo Wang [a,*], Zhouchuan Huang [a,*], Qin Wang [a,*], Dapeng Zhao [b], Xiumian Hu [a]

[a] State Key Laboratory of Critical Earth Material Cycling and Mineral Deposits, School of Earth Sciences and Engineering, Nanjing University, Nanjing, 210023, China
[b] Department of Geophysics, Graduate School of Science, Tohoku University, Sendai, 980-8578, Japan

ARTICLE INFO

Editor: J.P. Avouac

Keywords:
Seismic tomography
Tibetan plateau
Craton
Delamination
Mantle flow
Plateau expansion

ABSTRACT

The northeastern Tibetan Plateau (NE Tibet) is undergoing extensive outward expansion toward the Asian continent, generating significant intracontinental deformation. However, how the plateau and adjacent cratons respond to this process remains insufficiently understood. Here, we present refined three-dimensional P- and S-wave velocity models of the crust and upper mantle beneath NE Tibet, which provide new constraints on plateau-craton interactions. Prominent velocity contrasts in the upper mantle between the plateau (low velocities) and the adjacent blocks (high velocities) suggest that the plateau expansion has been, to first order, impeded by the surrounding blocks. However, several dipping high-velocity anomalies in the upper mantle indicate that parts of the cratonic lithosphere may have been disrupted, possibly in response to the extruded mantle flow from the plateau. Furthermore, a normal-to-low velocity zone in the upper mantle beneath the Qinling Orogen may represent an asthenospheric channel for the eastward extrusion of the Tibetan asthenosphere. A vertically extensive low-velocity anomaly from the surface to ~600 km depth beneath the Yinchuan-Hetao Graben around the Ordos Block may reflect an upper-mantle plume related to the plateau expansion. Our study confirms that both the plateau and its surrounding regions have responded significantly to the plateau expansion process during the India-Asia continental collision.

1. Introduction

The Tibetan Plateau, formed in response to the India-Asia collision since ~60 Ma (Ding et al., 2022; Hu et al., 2016), extends >1500 km from the Himalayan orogen to central Asia (Fig. 1a). It is characterized by high elevation (with an average elevation of >4000 m), thick crust (65–80 km), and widespread intracontinental deformation. A series of end-member models have been proposed to explain the formation and expansion of the Tibetan Plateau, including stepwise plateau growth through continental subduction coupled with lateral extrusion along several deep major strike-slip faults (Tapponnier et al., 2001), vertically coherent shortening of the whole lithosphere (England and Houseman, 1986), underthrusting of the Indian and/or Asian lithosphere beneath the Tibetan Plateau (Kind et al., 2002), and inflation by lateral channel flow in the mid-lower crust (Clark and Royden, 2000).

The northeastern Tibetan Plateau (NE Tibet) forms the leading edge of the Tibetan Plateau and plays a key role in the northward propagation of the India-Asia collision. NE Tibet is bounded by several cratons and ribbon microcontinents, which are, from west to east, the Tarim Basin to the west, the Alxa Block to the north, the Ordos Block to the northeast, and the Sichuan Basin to the southeast. A series of fault systems, such as the Altyn Tagh Fault, the Qilianshan-Nanshan thrust belt, the Haiyuan Fault, the Liupanshan Fault, and the Longmenshan Fault (Fig. 1a; Taylor and Yin, 2009; Zuza et al., 2016), are developed between the plateau and its adjacent tectonic units. Despite pronounced Cenozoic deformation within the Tibetan Plateau, deformation in the adjacent blocks, which belong to the North China Craton and the Yangtze Craton, remains comparatively weak.

Meanwhile, several orogens and basins have developed within NE Tibet. In the southwest, the Qaidam Basin forms a discrete block that contains >10 km-thick Cenozoic sedimentary sequences and records multiple Phanerozoic tectono-magmatic episodes (Cheng et al., 2021; Dong et al., 2022). At the northernmost margin, the northwest-trending Qilian Orogen is a Cenozoic reactivated belt that underwent Early Paleozoic orogeny followed by Mesozoic extension (Song et al., 2013; Yin and Harrison, 2000; Yu et al., 2021; Zuza et al., 2016). As the southeastern continuation of the Qilian Orogen, the Longzhong Basin has experienced subsidence since the Late Jurassic-Early Cretaceous

* Corresponding authors.
E-mail addresses: haibo.wang.seis@gmail.com (H. Wang), huangz@nju.edu.cn (Z. Huang), qwang@nju.edu.cn (Q. Wang).

https://doi.org/10.1016/j.epsl.2026.120004
Received 1 December 2025; Received in revised form 18 March 2026; Accepted 23 March 2026
Available online 1 April 2026

(Dong et al., 2022). To the east, the nearly east-west-trending Qinling Orogen was subjected to several stages of continental convergence among the North China Block, the South Qinling microplate, and the South China Block during the Paleozoic and Mesozoic (Dong and Santosh, 2016). The western Qinling Orogen is now incorporated into NE Tibet and is characterized by numerous scattered Cretaceous-Cenozoic basins overlying Late Proterozoic-Early Mesozoic oceanic and arc-type assemblages (Wang et al., 2023).

The Songpan-Ganze terrane, the southernmost triangular part of NE Tibet, is characterized by thick (~8 km on average) and widespread Triassic flysch deposits (Yin and Nie, 1993). It is generally regarded as a remnant ocean basin of the Paleo-Tethys Ocean trapped between converging continental blocks from the Late Paleozoic to Early Mesozoic (Tang et al., 2023). During the Late Triassic to Early Jurassic, the Songpan-Ganze flysch strata were thrust southeastward over the Yangtze Craton along the NE-trending Longmenshan thrust belt, leading to the formation of the western Sichuan foreland basin (Burchfiel et al., 1995; Liu et al., 2021). The Longmenshan thrust belt, consisting of several Neoproterozoic complexes and three NE-trending thrust faults, represents the reactivated western margin of the Yangtze Craton. It experienced uplift in the Late Triassic-Early Jurassic, wedge extrusion in the Early Cretaceous, and rapid exhumation since 40–30 Ma in response to the India-Asia continental collision (Xu et al., 2024).

Deep structures play a crucial role in plateau expansion and deformation. In recent years, many tomographic studies have investigated the seismic velocity structure of the crust and upper mantle beneath NE Tibet. Within the crust, the most prominent features include two low-velocity (low-V) zones located in the mid-lower crust beneath the Qilian Orogen and the junction zone between the northeastern Songpan-Ganze terrane and the western Qinling Orogen (e.g., Bao et al., 2020; Wang et al., 2017b). The lithosphere of NE Tibet is characterized by large-scale low-V anomalies, extending to depth of at least 200 km, as revealed by both P- and S-wave velocity (Vp, Vs) models (Zhang et al., 2018a, 2018b). In contrast, the surrounding regions, including the Alxa Block, the Ordos Block, and the Sichuan Basin, exhibit high-velocity (high-V) anomalies confined to the lower crust and upper mantle (e.g., Guo et al., 2022; Zhang et al., 2018a, 2018b). These observations indicate pronounced structural contrasts between the plateau and its surrounding blocks, as well as among different tectonic units within the plateau.

However, several key issues related to the plateau growth remain debated. Firstly, how were the structural heterogeneities within and around the plateau formed, and how do they influence subsequent plateau expansion? Secondly, although they are generally regarded as stable, how do the surrounding blocks or cratons respond to the outward growth of the plateau? In this study, we manually picked 156,563 P-wave and 93,014 S-wave arrivals from over 300 teleseismic events recorded by the dense seismic network (Fig. 1b), which were deployed by the ChinArray project and the China Earthquake Administration. We then jointly inverted the local arrival-time data and teleseismic relative arrival residuals to obtain refined three-dimensional (3-D) Vp and Vs models of the crust and upper mantle beneath NE Tibet and its adjacent areas, which provide new insights into the interactions between NE Tibet and the surrounding cratons.

2. Data and method

2.1. Local data

The local earthquake data used in this study were extracted from phase reports issued by the China Earthquake Administration, which contain P- and S-wave arrival times and hypocentral parameters of local earthquakes. To ensure data quality and adequate spatial coverage, we applied a multi-step selection process. First, we extracted earthquakes with magnitudes greater than 2.0 that had at least 8 recorded arrivals within the study area. To improve earthquake location accuracy, we defined the spatial extent of seismic stations using a polygon and excluded earthquakes outside this polygon.

We then relocated all local earthquakes with both P- and S-wave arrivals using Geiger's method (Zhao et al., 1992) and a one-dimensional (1-D) initial velocity model (Figure S1). The 1-D model is constructed by combining global and local models. The crust includes three layers. The intracrustal discontinuities are extracted from the CRUST1.0 model (https://igppweb.ucsd.edu/~gabi/rem.html), and the Moho depths are determined by receiver function studies (Wang et al., 2017a,b). The velocity in every layer is derived from a recent local tomographic model (Sun et al., 2021). In the upper mantle, we use the IASP91 Earth model (Kennett and Engdahl, 1991). This 1-D velocity model is also used as the starting model for the subsequent inversions. The uncertainties of the earthquake relocations are mostly smaller than 0.2 s in origin time and smaller than 2 km in space. In this study, we used the data from the events with small relocation uncertainties (i.e.,

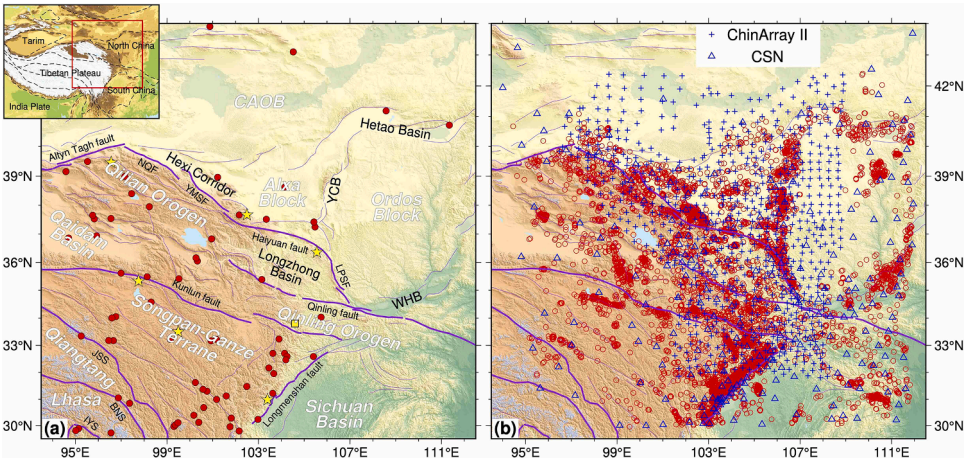

Fig. 1. Tectonic framework of northeast Tibet and surrounding regions (a), and seismic stations and local earthquakes used in this study (b). Thin purple lines indicate active faults, while thick purple lines highlight some major faults and suture zones (Taylor and Yin, 2009; Zuza et al., 2016). In (a), red dots and yellow stars denote the epicenters of earthquakes with magnitudes greater than 6.0 and 7.5, respectively. Earthquake data are from the ISC-GEM earthquake catalogue (Di Giacomo et al., 2018). The inset map shows the broader Tibetan Plateau, with the study area outlined by a red rectangle. In (b), blue open triangles and black crosses represent permanent (CSN) and temporary (ChinArray II) seismic stations, respectively. Red circles indicate local earthquakes included in this study. Abbreviations: CAOB – Central Asian Orogenic Belt, WHB – Weihe Basin, YCB – Yinchuan Basin, JSS – Jinsha suture zone, BNS – Bangong-Nujiang suture zone, IYS – Indus-Yalu suture zone, NQF – North Qilian fault, YMSF – Yumushan fault, LPSF – Liupanshan fault.

epicentral error <0.04°, focal depth error <5.0 km, and origin time error <0.4 s; Figure S2).

To obtain a relatively uniform spatial distribution of local earthquakes, we divided the study area into cubic cells with edge lengths of ~4 km and retained at most one event per cell. Only earthquakes with magnitudes >2.0 and at least 20 arrivals were considered. The event retained in each cell was chosen to maximize the number of recorded arrivals and the earthquake magnitude. In total, 7160 local earthquakes were selected from the initial phase reports. These earthquakes were recorded by 246 permanent seismic stations of the China Seismic Network (CSN; Fig. 1b) between January 2009 and September 2021, resulting in 144,669 P-wave and 115,646 S-wave arrivals.

2.2. Teleseismic data

Teleseismic arrivals used in this study were manually picked from seismograms recorded by 246 CSN permanent stations and 675 portable stations deployed during the ChinArray Phase II (ChinArray II; September 2013 to March 2015; Fig. 1b). We selected teleseismic events with epicentral distances between 30° and 90° and magnitudes greater than 5.5, yielding a dataset of >400 events. The waveforms were rotated from the North-East-Vertical coordinate system to the Radial-Transverse-Vertical coordinate system. P-wave signals were extracted from the vertical components and filtered using a Butterworth bandpass filter with corner frequencies of 0.1–0.5 Hz. Similarly, S-wave signals were extracted from the transverse components and filtered with a 0.04–0.2 Hz bandpass filter. Arrival times were measured using AIMBAT (Lou et al., 2013), a robust and efficient Python-based tool utilizing the multi-channel cross-correlation algorithm (VanDecar and Crosson, 1990) and enhanced by iterative cross-correlation and stacking procedures (Figure S3). In total, we obtained 156,563 P-wave arrivals from 334 events and 93,014 S-wave arrivals from 254 events (Fig. 2). Each teleseismic event was recorded by at least 10 stations, and most were recorded by >200 stations.

Crustal corrections were made to the teleseismic arrivals to remove travel-time delays caused by the 1-D crustal model adopted in this study (as described above; Figure S1) relative to the reference IASP91 model. We then computed relative travel-time residuals by subtracting, for each event, the mean residual across all stations. This procedure minimized biases arising from hypocentral mislocations, origin time uncertainties, and structural heterogeneities outside the study region (Figure S4; Chen et al., 2014; Zhao et al., 1994; See Text S1 for details). Figure S4 shows the spatial distributions of the mean relative residuals before and after the crustal corrections, together with the average crustal correction terms at stations with >10 recordings. The mean relative travel-time residuals of both P- and S-waves exhibit similar patterns, although the P-wave residuals are generally smaller than the S-wave residuals. Performing the crustal corrections reduced the amplitude of the residuals while preserving the first-order features of residual differences among stations. Strong negative residuals beneath the Sichuan Basin and the Ordos Block suggest prominent high-V anomalies in the underlying upper mantle, whereas strong positive residuals in NE Tibet and the Yinchuan-Hetao Basin likely indicate widespread low-V anomalies in those areas.

2.3. Method

The joint tomography method of Zhao et al. (1994) was applied to invert local arrival times and teleseismic relative residuals for separate 3-D Vp and Vs models. The velocity structure was parameterized on 3-D grid nodes with a lateral grid interval of 0.4° for Vp and 0.5° for Vs, and vertical nodes were set at depths of 10, 25, 40, 65, 100, 150, 200, 250, 300, 350, 400, 450, 500, 550, 600, 650, 700, and 750 km. Ray paths and theoretical travel times were computed using an efficient 3-D ray tracing method (Zhao et al., 1992), which accounts for curved velocity discontinuities and station elevations. The system of observation equations was solved using the conjugate-gradient-type LSQR algorithm (Paige and Saunders, 1982), incorporating both damping and smoothing regularizations. The adopted regularization parameters were determined empirically through extensive trial inversions with different combinations of damping and smoothing. The final parameter set was selected as a compromise solution that provided a substantial reduction in root-mean-square (RMS) travel-time residuals while maintaining a stable and reasonably smooth model. With this parameter set, the RMS was reduced from 0.601 s to 0.385 s for the final 3-D Vp model and from 0.906 s to 0.540 s for the final 3-D Vs model (Fig. 3; see Table S1 for details).

3. Analyses and results

3.1. Checkerboard resolution tests

Good ray path coverage is a prerequisite for obtaining a reliable tomographic model. The newly picked teleseismic arrivals substantially improve ray path coverage, leading to tomographic models with improved resolution beneath NE Tibet and its adjacent areas. Figures S4 and S5 show map views of hit counts (i.e., the number of rays passing through each grid node) for the P- and S-wave data, respectively. Most parts of the study area at all depths are well sampled, with hit counts exceeding 500. In particular, hit counts in the crust beneath the Longmenshan thrust belt are extremely high (>10,000) because of the intense seismicity there. In contrast, the southwestern part of the study

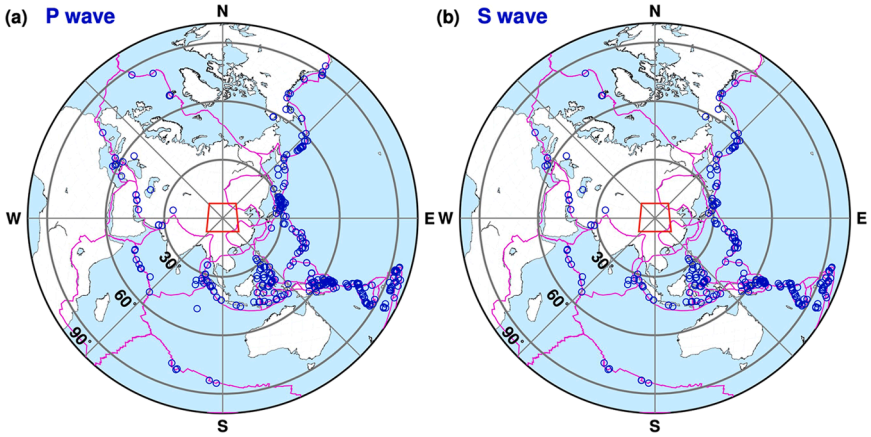

Fig. 2. Distribution of teleseismic events (blue circles; $M \geq 5.5$) used in this study for P-wave (a) and S-wave (b) tomography. Purple lines represent major plate boundaries (Bird, 2003), while red trapezoids outline the study region.

area is poorly sampled, owing to the sparse station distribution and the limited number of teleseismic events arriving from the southwest (Figs. 1b and 2).

We performed extensive checkerboard resolution tests (CRTs) to evaluate the ray coverage and spatial resolution of our 3-D Vp and Vs models (Zhao et al., 1992, 1994). Alternate positive and negative velocity anomalies (±4%) were assigned to the 3-D grid nodes to construct the input models. Synthetic travel-time residuals were then computed for these input models using the same earthquakes, seismic stations, and ray paths as in the real data set. Random Gaussian noise with a standard deviation of 0.1 s was added to the synthetic travel-time data to simulate pick errors in the arrival times. The synthetic data sets were subsequently inverted to obtain recovered images of the input checkerboard models. Figures S7 and S8 show CRT results with different lateral grid intervals (0.4°, 0.5°, and 0.6°) at selected depths, and Figures S9-S14 present several vertical cross-sections. The input models are well recovered in most parts of the study region at all depths, indicating that our tomographic models have a lateral resolution of ~50 km. At shallow depths (e.g., 10 and 25 km), only the central area covered by seismic stations is well recovered, because local earthquakes are concentrated beneath the station network (Fig. 1b) and teleseismic rays are nearly vertical beneath the stations. At greater depths (e.g., 200 – 700 km), most of the study region is well recovered, except for the southwestern part.

3.2. P- and S-wave velocity structures

The obtained Vp and Vs models reveal pronounced lateral heterogeneity beneath NE Tibet and adjacent areas (Figs. 4–10). The first-order patterns of the Vp and Vs models are broadly consistent, although the amplitudes of velocity anomalies and some small-scale features differ. Overall, Vs perturbations are larger in amplitude than the Vp perturbations. In contrast, the Vp model reveals more detailed structures, particularly several inclined high-V bodies in the upper mantle. This is because the P-wave arrivals are picked from higher-frequency waveforms (Figure S3) and there are more P-wave arrivals than the S-wave arrivals (Fig. 3). Hence, we infer that the Vp tomography reveals more detail of the crustal and upper-mantle structures beneath NE Tibet.

In the upper crust (10 km depth slices in Figs. 4 and 5), prominent low-V anomalies occur beneath major sedimentary basins, including the Yinchuan-Hetao Basin and the Sichuan Basin, reflecting the presence of relatively thick sedimentary sequences. In the middle-lower crust and uppermost mantle (40, 65, and 100 km depths in Figs. 4 and 5), strong velocity contrasts are observed along the plateau margin. Stable blocks (i.e., the Alxa Block, the Ordos Block, and the Sichuan Basin) are characterized by normal to high-V anomalies, whereas velocities within the plateau are relatively low. Two notable, distinct low-V anomalies are revealed in the crust beneath the northeastern Songpan-Ganze terrane and along the Qilian Orogen. In contrast, the Longzhong Basin, a small block within the plateau, exhibits normal-to-high velocity anomalies throughout the lower crust and uppermost mantle (Figs. 4 and 5).

In the upper mantle, the Vp and Vs models display relatively simple structures (Figs. 4 and 5). High-V anomalies are imaged beneath the Alxa Block, the Ordos Block, and the Sichuan Basin, whereas a large-scale low-V anomaly is observed beneath NE Tibet and extends down to ~300 km depth. The high-V anomaly beneath the Alxa Block is relatively weak and small, and vanishes at ~300 km depth (Figs. 4–6). The high-V anomaly beneath the southern and central parts of the Ordos Block extends down to ~500 km depth in the Vp model and to ~400 km depth in the Vs model (Figs. 4, 5, and 7). The high-V anomaly beneath the Sichuan Basin is strong and persists to ~300 km depth (Figs. 4, 5, and 8). A slab-like high-V anomaly is imaged in the upper mantle beneath the northeastern Songpan-Ganze terrane and the western Qinling Orogen. This anomaly is connected to the high-V zone beneath the Sichuan Basin, dips west-northwestward, and reaches the upper part of the mantle transition zone (MTZ; Fig. 8). A distinct E-W striking gap beneath the North Qinling Orogen separates the Ordos Block and the Sichuan Basin. This gap is ~150 km wide and spans depths of ~150–300 km (Figs. 4, 5, and 9).

Within the MTZ and the uppermost lower mantle, an N-S striking high-V anomaly is imaged along ~100°E at depths of 500–700 km (Figs. 4 and 5). A low-V anomaly is also visible beneath the northern Sichuan Basin and the southern Qinling Orogen (Figs. 4 and 5). Beneath the Yinchuan-Hetao Basin, a pronounced low-V anomaly appears as a narrow zone in the crust, widens into the north Ordos Block at 100–400 km depth, and extends to the northwest of the study region at 500–600 km depth (Figs. 4, 5, and 10).

3.3. Restoring resolution tests

To further evaluate the robustness of the main features of our tomographic models and assess possible smearing effects, we conducted a series of restoring resolution tests (RRTs). In the RRTs, the input models were derived from the final tomographic results, and all other procedures followed those used in the CRTs. In the first set of RRTs (Figures S15 and S16), the final tomographic images are directly used as the input models. These input models were fully recovered, implying that the inversion method is stable and the data sets are capable of resolving the crust and upper mantle structure beneath NE Tibet and adjacent areas. In the second set (Figures S17 and S18), the input models retained only the obtained structures above a given depth (200, 300, 400, 500, 600, and 700 km) to test possible vertical smearing effects. The overall patterns can be well recovered; however, smearing does occur, especially in the peripheral regions. Vertical smearing beneath the central part of the study area is negligible because the affected features are small in scale and have relatively low amplitudes.

In the third set of RRTs, the input model contained a simplified representation of the major upper mantle features: a large-scale low-V anomaly beneath NE Tibet, a vertically elongated low-V anomaly beneath the Yinchuan-Hetao Graben, two separate high-V anomalies beneath the Ordos Block and the Sichuan Basin, and a west-northwest-dipping high-V anomaly beneath the Songpan-Ganze terrane and the western Qinling Orogen (Figure S19). We then modified the input models by narrowing the gap between the high-V zones beneath the Ordos Block and the Sichuan Basin and removing the west-northwest-dipping high-V anomaly (Figure S20), or by thinning these anomalies (Figure S21). These recovered images indicate that the first-order features are robust: neither the gap between the Ordos Block and the Sichuan Basin nor the west-northwest-dipping high-V anomaly beneath the Songpan-Ganze terrane and the western Qinling Orogen can be attributed to inversion artifacts.

4. Discussion

4.1. Comparison with previous tomographic results

Several regional tomographic models have been published for NE Tibet and its surrounding areas (e.g., Bao et al., 2020; Guo et al., 2022; Li et al., 2017; Zhang et al., 2018a,b). Despite differences in data coverage, inversion strategies, and parameterizations, these studies consistently resolve a set of robust first-order structures. Our Vp and Vs models reproduce these key features: large-scale low-V anomalies dominate the entire crust and upper mantle beneath the plateau, whereas high-V lithosphere underlies the Alxa Block, the Ordos Block, and the Sichuan Basin. These broad patterns are consistent with the results of Zhang et al. (2018a,b).

Compared with Zhang et al. (2018a, 2018b), our joint inversion of local and teleseismic data provides improved structural details above ~100 km depth. In the middle-lower crust and uppermost mantle, the low-V anomalies within the plateau do not appear as a single coherent body; instead, they divide into two large-scale low-V zones: one beneath the Qilian Orogen and the other beneath the northeastern

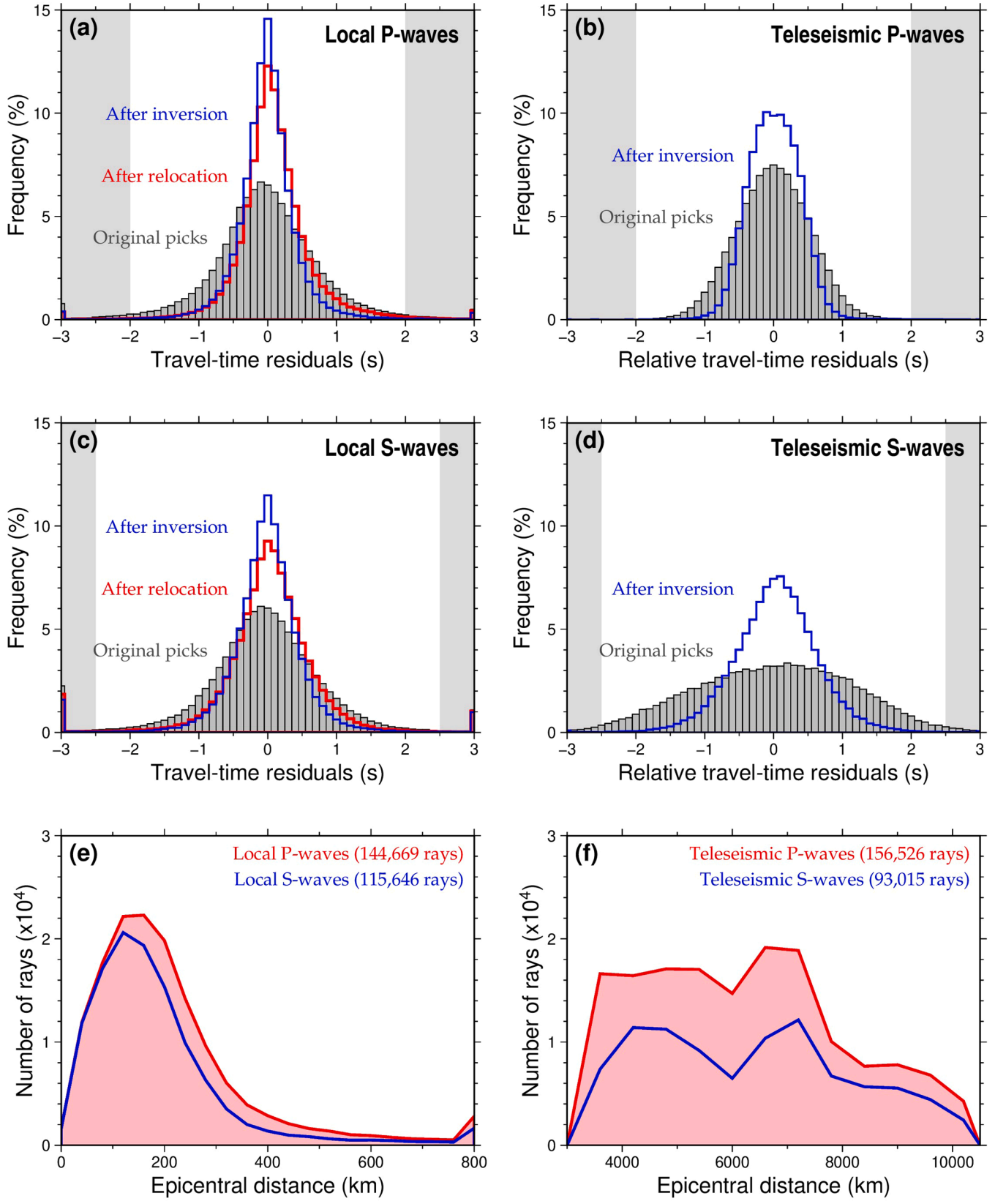

Fig. 3. Information on the seismic rays used in this study. Distribution of local P- (a) and S-wave (c) travel-time residuals for the original picks (gray bars), after relocation (red lines), and after the tomographic inversions (blue lines). Distribution of teleseismic P- (b) and S-wave (d) relative travel-time residuals for the original picks (gray bars) and after the tomographic inversions (blue lines). The gray patches near the margins in panels (a)-(d) denote outliers excluded during the inversions. Panels (e) and (f) show the numbers of local and teleseismic rays used to determine the final tomographic model as a function of epicentral distance, respectively.

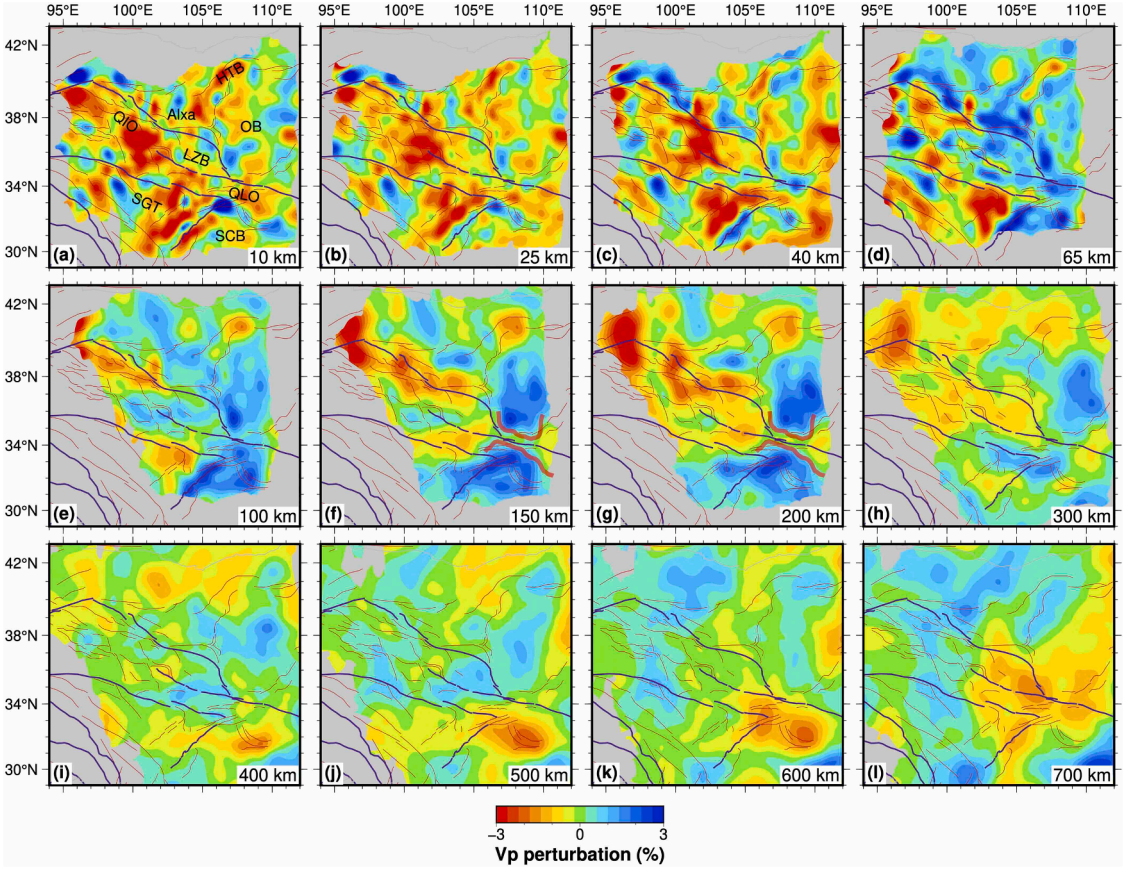

Fig. 4. Map views of the obtained P-wave tomographic model at selected depths. The depth of each layer is indicated at the lower-right corner of each panel. Blue and red colors denote positive and negative velocity perturbations, respectively, with the scale shown at the bottom. Thin red lines and thick purple lines denote active faults (Taylor and Yin, 2009; Zuza et al., 2016). Thick red lines in panels (f) and (g) mark the asthenosphere channel (Yu et al., 2021b). Abbreviations: SCB – Sichuan Basin, OB – Ordos Block, SGT – Songpan-Ganze Terrane, QLO – Qinling Orogen, QIO – Qilian Orogen, Alxa – Alxa Block, LZB – Longzhong Basin, HTB – Hetao Basin.

Songpan-Ganze terrane and the western Qinling Orogen. In addition, the Longzhong Basin is characterized by normal-to-high velocities in the lower crust and uppermost mantle. These features are also suggested by regional surface wave tomography (e.g., Bao et al., 2020; Li et al., 2017; Wang et al., 2017b).

Relative to the surface wave models (e.g., Bao et al., 2020; Li et al., 2017; Wang et al., 2017b) and the teleseismic-only Vp and Vs models (Zhang et al., 2018a,b), our joint local-teleseismic inversion, combined with a substantially expanded teleseismic dataset, provides tighter constraints on the vertical extent and downward continuation of the shallow anomalies (Figs. 4–8 and S22-S24). While confirming major features revealed by previous studies (e.g., Guo et al., 2022; Yu et al., 2021b; Zhang et al., 2018a,b), our models resolve finer details due to the improved teleseismic ray coverage. For example, a west-northwest-dipping high-V zone beneath the northeastern Songpan-Ganze terrane and the western Qinling Orogen is resolved as a robust feature in our results.

These comparisons demonstrate that the first-order structural pattern, characterized by extensive low-V anomalies beneath the plateau and strong high-V lithospheric roots beneath the surrounding cratonic blocks, is highly reproducible across different datasets and methodologies. The improved resolution of our dataset sharpens lithospheric boundaries and reveals upper mantle structures that were previously obscured. These newly resolved features provide fresh constraints on the mechanical interaction between NE Tibet and the adjacent stable blocks, which we further discuss in the following sections on geodynamic implications.

4.2. *Asia-Tibet interactions beneath NE Tibet*

Whether the surrounding Asian blocks have subducted or underthrusted beneath NE Tibet remains debated. In the northern and eastern margins of NE Tibet, teleseismic receiver function studies in the western Qilian Orogen and Longzhong Basin regions reached completely opposite conclusions (Shen et al., 2015; Ye et al., 2015. Our new tomography reveals pronounced lateral velocity contrasts between NE Tibet and the surrounding blocks, including the Alxa Block and the Ordos Block (Figs. 4–7).

Along profiles crossing the western Qilian Orogen and the Alxa Block (profiles AA', BB', and CC' in Fig. 6), a prominent large-scale low-V anomaly is imaged beneath the Qilian Orogen, extending to ~300 km depth. The low-V zone extends beneath the whole block under the western Alxa Block (profiles AA' and BB' in Fig. 6) but is restricted by the high-V body in the upper mantle under the eastern Alxa Block (profiles CC' and DD' in Fig. 6). There are also apparent south-dipping high-V bodies in the upper mantle (profiles BB' and CC' in Fig. 6), similar to those revealed by Wang et al. (2022). To the east, along profiles crossing the Longzhong Basin and the Alxa or Ordos Blocks (profile DD' in Fig. 6 and profiles AA', BB', and CC' in Fig. 7), a ~50 km thick, weak high-V zone is imaged in the uppermost mantle beneath the Longzhong Basin, sandwiched between crustal low-V anomalies above and large-scale upper mantle low-V anomalies below. Given its modest amplitude and relatively flat geometry, we interpret this weak high-V body as in-situ lithospheric mantle rather than subducted or underthrust continental lithosphere. Taken together, these observations argue against large-scale subduction or underthrusting of the Asian

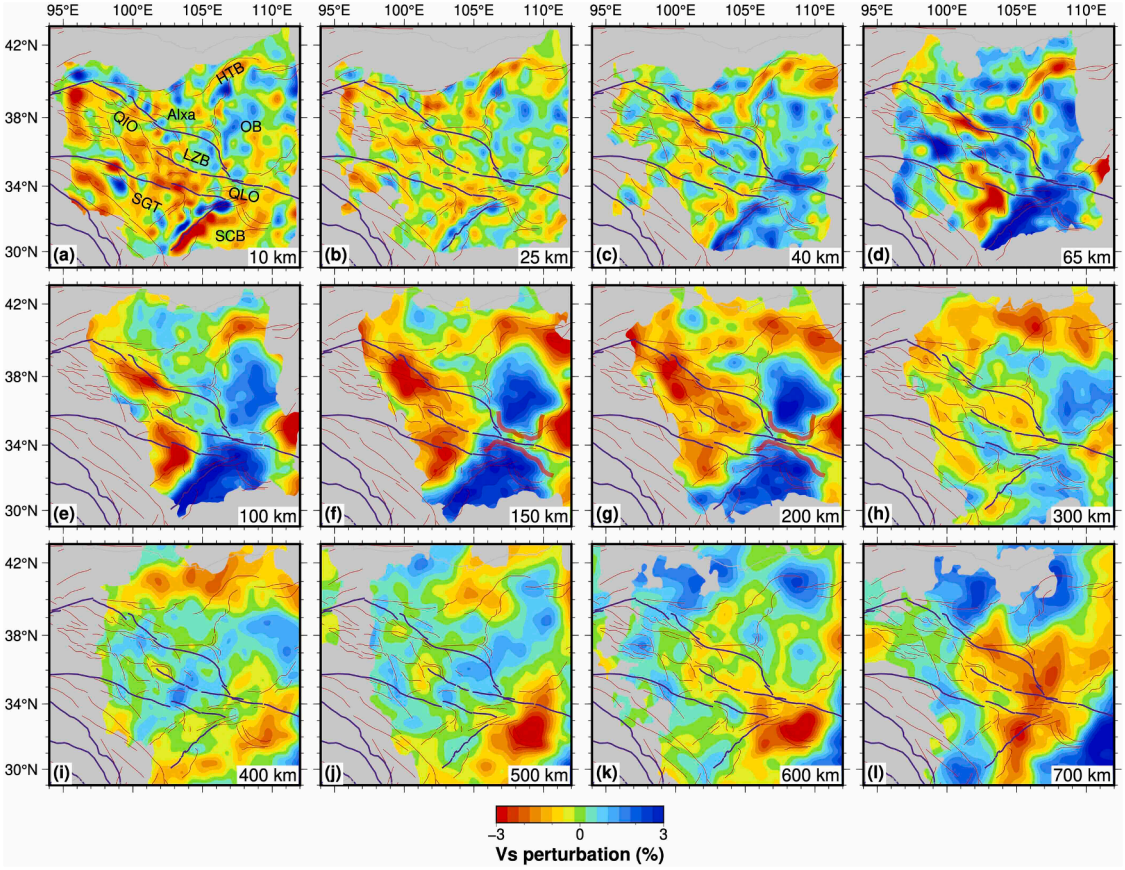

Fig. 5. Similar to Fig. 4 but for S-wave tomography.

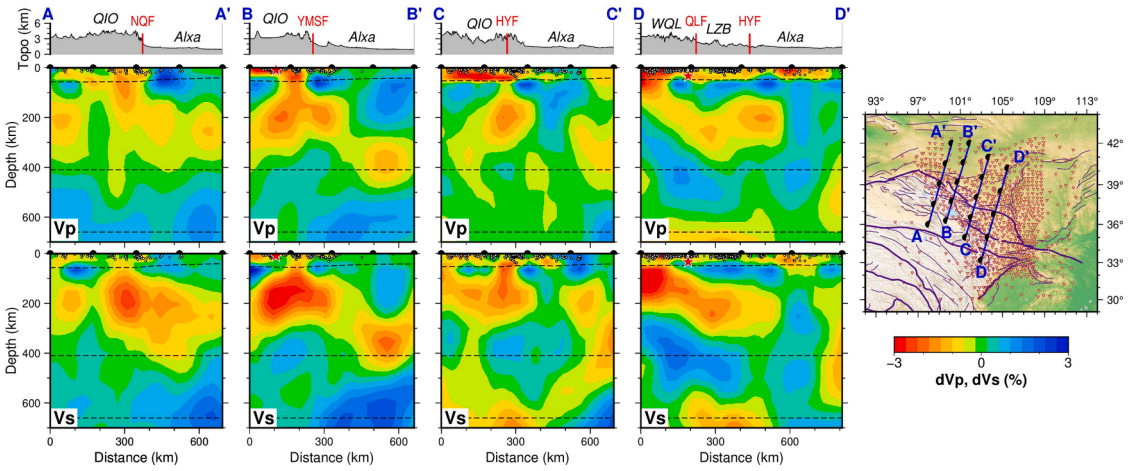

Fig. 6. Vertical cross-sections of P- and S-wave tomography along four profiles crossing northeast Tibet and its northern margins, as indicated in the inset map. Each panel, from top to bottom, shows the topography, P-wave tomography, and S-wave tomography. Vertical bars on the topography mark the locations of major active faults, and major geological units are labeled. Dashed lines in each cross-section denote the Moho (Wang et al., 2017a,b), the 410-km, and 660-km discontinuities. White dots indicate local seismicity within ±15 km of each profile. Red triangles in the inset map denote seismic stations. Abbreviations: NQF – North Qilian fault, YMSF – Yumushan fault, HYF – Haiyuan fault, QLF – Qinling fault, QIO – Qilian Orogen, Alxa – Alxa Block, LZB – Longzhong Basin, WQL – western Qinling Orogen.

lithosphere beneath NE Tibet, although localized underthrusting cannot be ruled out in specific boundary zones.

There are additional observations and geophysical constraints that support this interpretation. First, intermediate-depth earthquakes are absent. Upper mantle seismicity is commonly observed where one continental plate underthrusts or subducts beneath another, such as beneath the southern Lhasa terrane (e.g., Schulte-Pelkum et al., 2019), the Burman arc (e.g., Kumar et al., 2015), and the Pamir-Hindu Kush (e.g., Sippl et al., 2013). In our study, the distribution of local earthquakes plotted along the vertical cross-sections (white dots in Figs. 6 and 7) shows that all events are confined to the crust, and most occur at depths shallower than 20 km. Second, migration images derived from P-wave receiver functions indicate that the crust beneath NE Tibet is thickened and exhibits complex internal structures, whereas the adjacent blocks have thinner crust, a relatively flat Moho, and simple internal structures (e.g., Zhang et al., 2020). In addition, migration images derived from

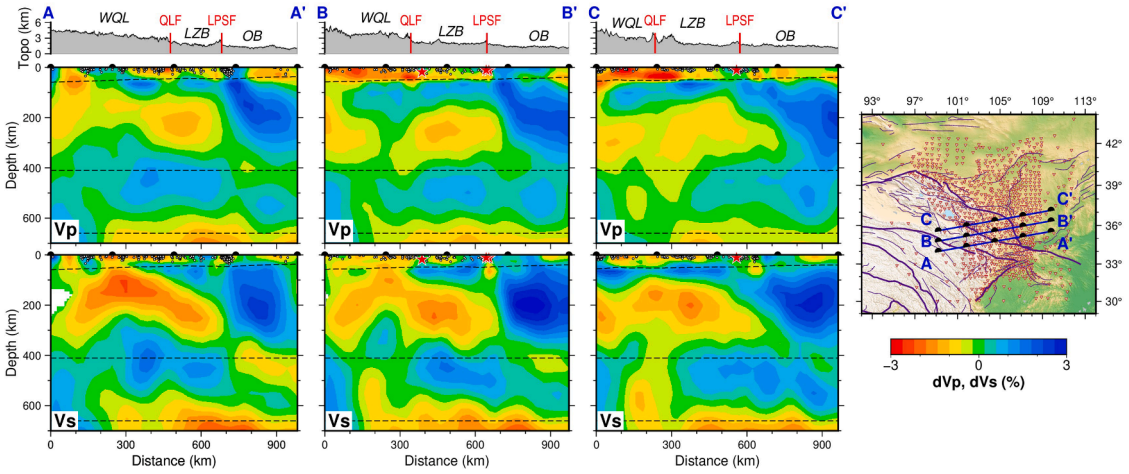

Fig. 7. Similar to Fig. 6, but along three vertical cross-sections crossing northeast Tibet and the Ordos Block. Abbreviations: QLF – Qinling fault, LPSF – Liupanshan fault, WQL – western Qinling Orogen, LZB – Longzhong Basin, OB – Ordos Block.

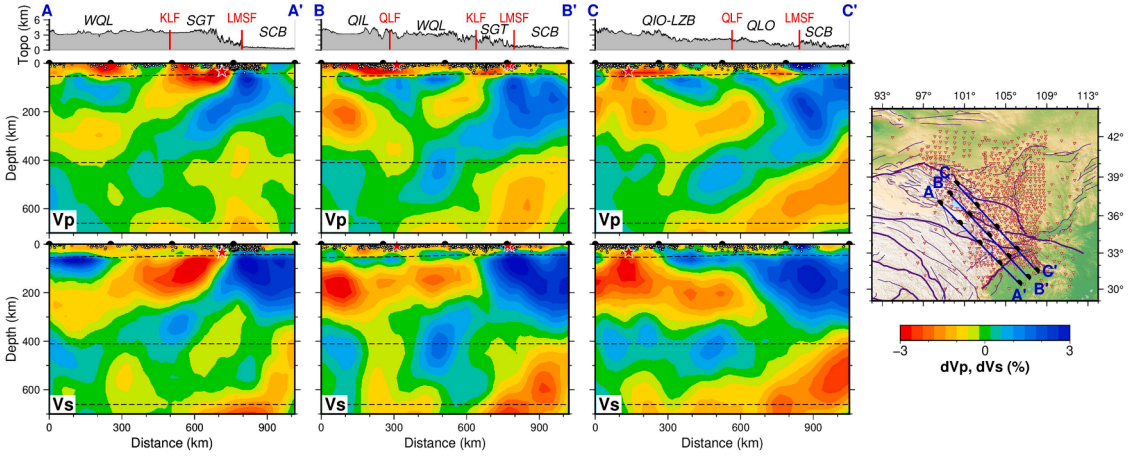

Fig. 8. Similar to Fig. 6, but along three vertical cross-sections crossing northeast Tibet and the Sichuan Basin. Abbreviations: KLF – Kunlun fault, LMSF – Longmenshan fault, QLF – Qinling fault, WQL – western Qinling Orogen, QIO – Qilian Orogen, SGT – Songpan-Ganze terrane, LZB – Longzhong Basin, SCB – Sichuan Basin.

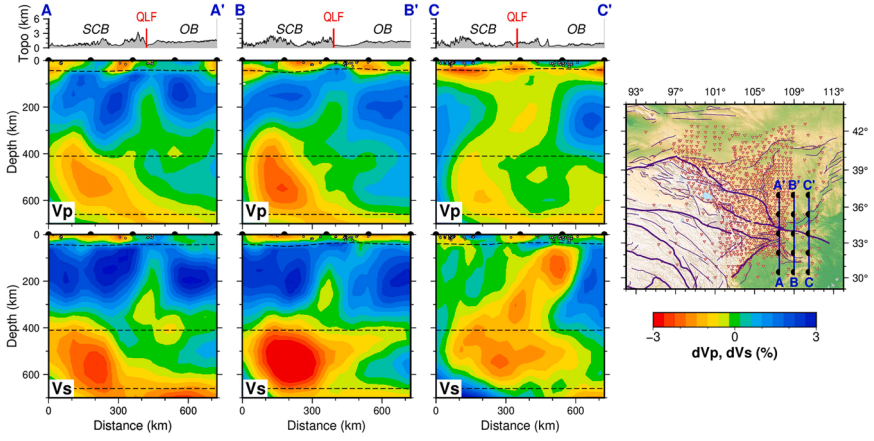

Fig. 9. Similar to Fig. 6, but along three vertical cross-sections crossing the Sichuan Basin and Ordos Block. Abbreviations: QLF – Qinling fault, SCB – Sichuan Basin, OB – Ordos Basin.

S-wave receiver functions reveal that the lithosphere-asthenosphere boundary (LAB) within the plateau is diffuse, whereas the LAB in the surrounding blocks is sharp and flat (Shen et al., 2015; Xu et al., 2019; Zhang et al., 2020).

Notably, the western Qilian Orogen and the Longzhong Basin exhibit markedly different surface deformation patterns. The western Qilian

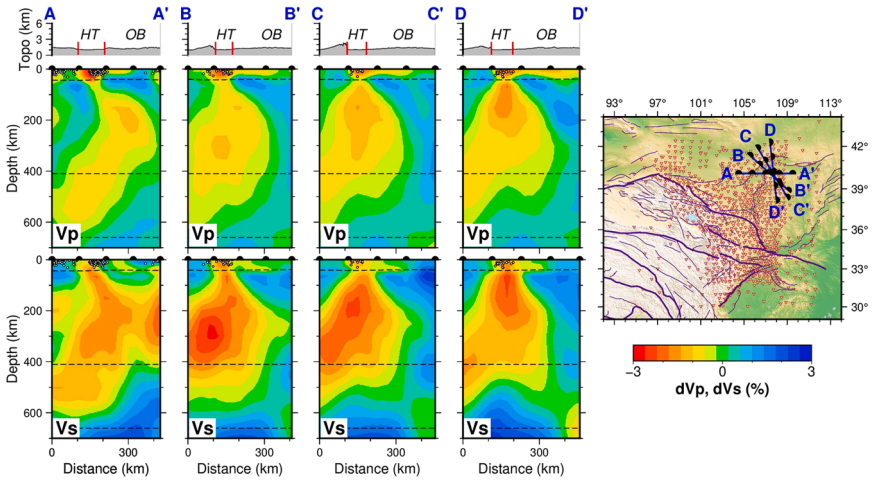

Fig. 10. Similar to Fig. 6, but along three vertical cross-sections crossing the Yinchuan-Hetao Graben. Abbreviations: HT – Hetao Basin, OB – Ordos Basin.

Orogen forms a broad WNW-trending fold-thrust belt, characterized by high elevation (average ~4 km), steep topographic relief, and a thick foreland basin to its north. In contrast, the Longzhong Basin consists of a series of shallow intermontane basins with generally low topographic gradients (Ren et al., 2024). Furthermore, the magnitude of Cenozoic crustal shortening in the western Qilian Orogen (~50%) significantly exceeds that in the Longzhong Basin (<15%; Zuza et al., 2016, and references therein). Our tomographic results reveal contrasting seismic structures within the lower crust and uppermost mantle beneath the two regions. A pronounced low-V anomaly beneath the western Qilian Orogen extends continuously from the crust down to ~300 km depth (Figs. 4–7). This low-V anomaly, also detected by surface wave tomography (e.g., Li et al., 2017; Wang et al., 2017b), may reflect a warm and mechanically weak lithosphere produced by a combination of shear heating along major faults, localized asthenosphere upwelling, and crustal radiogenic heating (Wang et al., 2017b). In contrast, the lower crust and uppermost mantle beneath the Longzhong Basin exhibit normal-to-high seismic velocities (65 and 100 km depth slices in Figs. 4 and 5, profile DD' in Fig. 6, and Fig. 7), indicative of a relatively cold and stable lithosphere. These contrasting lithospheric properties likely play a fundamental role in shaping the distinct surface deformation styles observed in the two regions (Ren et al., 2024). Thermochronological and sedimentological records show that the western Qilian Orogen experienced an episode of accelerated crustal shortening during the Middle Miocene (ca. 15–10 Ma), with deformation progressively propagating outward and reaching the Longzhong Basin in the Late Miocene (<10 Ma; Yu et al., 2023). This diachronous deformation between the western Qilian Orogen and the Longzhong Basin further supports the interpretation that the lithospheric strength contrasts may play a controlling role in temporally distinct stages of plateau expansion.

4.3. *Delaminated lithospheric mantle or a relic slab beneath NE Tibet*

An important feature in our tomographic images is the slab-like high-V anomaly in the upper mantle beneath the northeastern Songpan-Ganze terrane and the western Qinling Orogen. This high-V body is connected to the high-V zone beneath the Sichuan Basin, dips west-northwestward, and extends into the upper part of the MTZ (Figs. 4, 5, and 8). Above it, a distinct low-V anomaly is observed in the middle-lower crust and uppermost mantle. This low-V anomaly has been repeatedly imaged by surface wave tomography (e.g., Bao et al., 2020; Wang et al., 2017b), body wave tomography (e.g., Sun et al., 2021; Zhang et al., 2018a, 2018b), and joint inversion of receiver functions and surface wave dispersions along dense linear arrays (Deng et al., 2018). These studies interpreted the low-V anomaly in the middle-lower crust and uppermost mantle as being related to asthenospheric upwellings and/or lateral asthenospheric flow induced by delamination of a thick lithospheric root (e.g., Xu et al., 2019), which implicitly requires a detached lithospheric mantle at greater depths. Because of the limited depth extent of their models, however, the delaminated lithospheric mantle itself could not be resolved. Our tomography extends to the MTZ and reveals a slab-like high-V anomaly directly beneath the previously documented low-V body. The restoring resolution tests (Section 3.3) have confirmed that this feature is robust. We interpret this slab-like high-V body as the delaminated lithospheric mantle formed during the Cenozoic, based on its morphology, depth range, and spatial correlation with the overlying low-V anomaly.

In addition to seismic velocity investigations, several independent observations support this scenario. Xu et al. (2019) imaged the LAB beneath NE Tibet and found that the LAB beneath the northeastern Songpan-Ganze terrane and the western Qinling Orogen is notably shallow (~107–115 km). Li et al. (2020) derived a two-dimensional thermal structure across the northeastern Songpan-Ganze terrane using magnetotelluric (MT) data and interpreted a large-scale upper mantle conductor as a zone of partial melting with temperatures of 1300–1500 °C and melt fractions up to 10%. Xia et al. (2023) further identified a relatively thin thermal lithosphere (<100 km) and high surface heat flow (>70 mW/m^2) in this region based on a new thermal-isostasy method. Collectively, receiver-function, MT, and geothermal studies indicate that the lithosphere beneath the northeastern Songpan-Ganze terrane is thin and thermally weakened, consistent with a lithosphere that has undergone delamination. Furthermore, based on multiple geodetic datasets and climate models, Zhang et al. (2021) inferred that the crust of NE Tibet is uplifting, with a Moho uplift rate of 2.7 ± 1.3 mm/yr. The Moho uplift may reflect isostatic adjustment following the removal of a thickened lithospheric root.

In addition, Miocene potassic volcanic rocks in the western Qinling Orogen (the yellow square in Fig. 1a) exhibit high Mg#, suggesting a mantle-derived origin and a possible link to asthenospheric upwellings associated with lithospheric delamination (Dai et al., 2018; Mo et al., 2006). Taking the Miocene magmatic event as a rough marker for the onset of delamination, and considering the present position of the slab-like high-V anomaly (Fig. 8), we estimated the sinking rate of the delaminated lithosphere to be ~15 mm/yr. This rate is comparable to estimates for delamination in southeastern Tibet (20 ± 5 mm/yr; Feng et al., 2022) and central Tibet (~15 mm/yr; Chen et al., 2017), and is consistent with numerical models (Peng et al., 2022).

However, an alternative model of plate subduction may also explain some features of the seismic images. Although Cenozoic volcanic rocks

occur in the western Qinling Orogen as mentioned above, they are rare in this region. The observed Moho uplift and surface exhumation could be attributed solely to the outward expansion of the plateau. The relatively warm and thin lithosphere may result from lateral asthenospheric flow originating from the central Tibetan Plateau. Slab-like high-V anomalies in the upper mantle are commonly interpreted as fossil or stagnant slabs, as observed beneath western North America (Dougherty et al., 2020) and the eastern Anatolia Plateau (Portner et al., 2018). The Songpan-Ganze terrane and the western Qinling Orogen were amalgamated together during the Paleozoic to Early Mesozoic (Dong and Santosh, 2016). The final episode of subduction in this region involved the north-northwestward subduction of the Mianlue Ocean, which was completely consumed no later than the Late Triassic (Dong and Santosh, 2016). If the slab-like high-V anomaly represents a relic slab, it would correspond to the remnant of the Mianlue Ocean slab subducted during the Late Triassic. However, a viable mechanism is required to explain how such a structure could have been preserved in the upper mantle for over 200 million years.

4.4. Eastward asthenospheric flow beneath the Qinling Orogen

An increasing number of studies have highlighted the importance of an asthenospheric flow channel that facilitates the eastward extrusion of upper mantle materials from the plateau (e.g., Schellart et al., 2019). Based on an E-W fast-polarization direction of relatively strong seismic anisotropy derived from shear wave splitting measurements, Huang et al. (2008) first suggested eastward upper-mantle flow beneath the Qinling Orogen. Subsequent studies using expanded datasets from both permanent and temporary seismic stations have supported this interpretation (e.g., Guo et al., 2022; Yu et al., 2021b; Yu and Chen, 2016). Benefiting from wider and denser station coverage, along with the large number of newly manually picked teleseismic arrivals, our new Vp and Vs models provide unprecedentedly tight constraints on this normal-to-low channel in the upper mantle. The results identified a normal-to-low velocity gap at depths of 150–300 km between the high-V anomalies beneath the Ordos Block and the Sichuan Basin (Figs. 4, 5, and 9). Analogue modelling experiments suggested that the eastward asthenosphere channel may result from the combined effects of continuous India-Eurasia convergence and the retreat of the subducting Pacific Plate (Schellart et al., 2019). In addition, the eastward-flowing asthenospheric material may further influence the lithospheric reworking of the North China Craton (e.g., Guo et al., 2022; Huang et al., 2008).

4.5. A plume beneath the Yinchuan-Hetao Graben?

The Yinchuan-Hetao Graben is a Cenozoic rift, located to the northwest of the Ordos Block (Fig. 1a). Subsidence began in the Oligocene and accelerated during the Neogene (Zhang et al., 1998). The graben contains thick sedimentary deposits, with an average thickness exceeding 5 km and a maximum thickness of ~15 km (Li et al., 2022). Many end-member models have been proposed to explain the formation mechanism of the Yinchuan-Hetao Graben. The first model interprets the graben as a back-arc basin, attributing its formation to the westward subduction of the Pacific Plate and associated back-arc extension (Zhu et al., 2011). The second model attributes the graben formation to differential movement of adjacent blocks along a strike-slip boundary fault, driven by northeastward expansion of the Tibetan Plateau (Zhang et al., 2007). The third model interprets the basin as an active graben resulting from asthenospheric upwelling (e.g., Tian et al., 2011).

Our refined tomographic images reveal that a pronounced low-V anomaly beneath the Yinchuan-Hetao Graben extends from the surface to ~600 km depth and dips northwestward (Figs. 4, 5, and 10), suggesting significant mantle upwelling from the MTZ. The asthenospheric upwelling can induce elevated temperature and partial melting in the upper mantle, manifesting as low-Vp and low-Vs anomalies. The MTZ topography derived from receiver functions shows a depressed 410 km discontinuity and an approximately flat 660 km discontinuity beneath this region (Huang et al., 2022; Liu et al., 2022). The depression of the 410 km discontinuity is generally attributed to an increase in temperature at that depth (e.g., Agius et al., 2017). Therefore, the thinned MTZ supports the interpretation of thermal upwelling from the MTZ, which may present the deep origin of the Yinchuan-Hetao Graben.

4.6. Implications for the plateau growth

Our new tomographic models suggest that plateau growth in NE Tibet is governed primarily by lateral variations in lithospheric strength and localized mantle dynamics, rather than by large-scale underthrusting of the surrounding Asian blocks. Extensive low-V anomalies beneath the plateau indicate a warm, weak lithosphere that facilitates distributed deformation, whereas high-V lithospheric roots beneath the Alxa, Ordos, and Sichuan blocks act as rigid barriers that impede outward expansion (e.g., Zhang et al., 2018b; Shen et al., 2015). This mechanical contrast helps explain the strong spatial differences in deformation between the western Qilian Orogen and the Longzhong Basin, as well as the diachronous outward propagation of shortening since the Miocene (e.g., Ren et al., 2024). At the same time, lithospheric delamination beneath the northeastern Songpan-Ganze terrane and western Qinling, together with eastward asthenospheric flow and mantle upwelling beneath the Yinchuan-Hetao Graben, indicates that deep mantle processes have contributed to weakening the lithosphere and promoting localized uplift, extension, and edge growth of the plateau.

5. Conclusion

New 3-D Vp and Vs tomographic models of the crust and upper mantle beneath the northeastern Tibetan Plateau were obtained through the joint inversion of arrival times of local earthquakes and teleseismic relative travel-time residuals recorded by CSN and ChinArray II. The large number of newly manually picked teleseismic arrival times significantly enhance the resolution of both Vp and Vs models, providing new insights into the geodynamics of NE Tibet and its surrounding regions. The main findings of this study are summarized as follows.

1. The continental blocks surrounding NE Tibet, including the Alxa Block, the Ordos Block, and the Sichuan Basin, appear as high-V anomalies extending to at least ~300 km depth in both Vp and Vs models. The well-defined velocity boundaries among these blocks and the plateau do not favor large-scale subduction or underthrusting of the Asian lithosphere beneath NE Tibet. Instead, they act as barriers that partially constrain the movement and deformation within the plateau.
2. Lateral variations in the upper-mantle seismic structures are also notable along the margin of NE Tibet. A prominent low-V anomaly continuously extends from the crust to ~300 km depth beneath the western Qilian Orogen, indicating a warm and mechanically weak lithosphere there. In contrast, a high-V layer in the uppermost mantle, sandwiched between low-V anomalies in the crust and upper mantle, suggests a relatively cold and strong lithosphere beneath the Longzhong Basin. This lateral variation may result from the inherited structures or different evolutionary stages related to the outward expansion of the Tibetan Plateau.
3. A northwestward-dipping high-V anomaly is identified at depths of 200–500 km beneath the northeastern Songpan-Ganze terrane and the western Qinling Orogen, and it is connected to the high-V zone beneath the Sichuan Basin. This feature may represent delaminated lithospheric mantle since ~20 Ma or a remanent slab retained in the upper mantle.
4. An ~100 km wide normal-to-low velocity gap at depths of 150–300 km beneath the Qinling Orogen separates the high-V roots of the Ordos Block and the Sichuan Basin. This gap may represent an

eastward asthenospheric extrusion channel, allowing mantle flow from NE Tibet to the North China Craton.

5. A large-scale low-V anomaly extends from the MTZ to the crust beneath the Yinchuan-Hetao Graben, implying that the Yinchuan-Hetao Graben is an active rift caused by an upper-mantle plume.

CRediT authorship contribution statement

Haibo Wang: Writing – review & editing, Writing – original draft, Visualization, Validation, Methodology, Investigation, Formal analysis, Data curation, Conceptualization. **Zhouchuan Huang:** Writing – review & editing, Writing – original draft, Methodology, Funding acquisition, Formal analysis, Data curation, Conceptualization. **Qin Wang:** Writing – review & editing, Investigation, Formal analysis. **Dapeng Zhao:** Writing – review & editing, Software, Methodology, Investigation. **Xiumian Hu:** Writing – review & editing, Investigation, Formal analysis.

Declaration of competing interest

The authors declare that they have no known competing financial interests or personal relationship that could have appeared to influence the work reported in this paper.

Acknowledgment

The waveforms used are provided by the Data Management Center of the China National Seismic Network at the Institute of Geophysics (SEISDMC, doi: 10.11998/SeisDmc/SN). This research was funded by the National Natural Science Foundation of China (U22B6002, 42204094, 42174056). Most figures were created using the free software GMT (Wessel et al., 2019). The numerical calculations were conducted using the resources of the High-Performance Computing Center at Nanjing University. We thank Prof. Jean-Philippe Avouac (the Editor) and two anonymous reviewers for their very helpful and constructive comments.

Supplementary materials

Supplementary material associated with this article can be found, in the online version, at doi:10.1016/j.epsl.2026.120004.

Data availability

The authors do not have permission to share data.

References

Agius, M.R., Rychert, C.A., Harmon, N., Laske, G., 2017. Mapping the mantle transition zone beneath Hawaii from Ps receiver functions: evidence for a hot plume and cold mantle downwellings. Earth. Planet. Sci. Lett. 474, 226–236. https://doi.org/10.1016/j.epsl.2017.06.033.

Bao, X., Song, X., Eaton, D.W., Xu, Y., Chen, H., 2020. Episodic lithospheric deformation in eastern Tibet inferred from seismic anisotropy. Geophys. Res. Lett. 47. https://doi.org/10.1029/2019GL085721 e2019GL085721.

Bird, P., 2003. An updated digital model of plate boundaries. Geochem. Geophys. Geosyst. 4. https://doi.org/10.1029/2001GC000252, 2001GC000252.

Burchfiel, B.C., Zhiliang, C., Yupinc, L., Royden, L.H., 1995. Tectonics of the Longmen Shan and adjacent regions, Central China. Int. Geol. Rev. 37, 661–735. https://doi.org/10.1080/00206819509465424.

Chen, C., Zhao, D., Wu, S., 2014. Crust and upper mantle structure of the New Madrid Seismic Zone: insight into intraplate earthquakes. Phys Earth Planet. Inter. 230, 1–14. https://doi.org/10.1016/j.pepi.2014.01.016.

Chen, M., Niu, F., Tromp, J., Lenardic, A., Lee, C.-T.A., Cao, W., Ribeiro, J., 2017. Lithospheric foundering and underthrusting imaged beneath Tibet. Nat. Commun. 8, 15659. https://doi.org/10.1038/ncomms15659.

Cheng, F., Jolivet, M., Guo, Z., Wang, L., Zhang, C., Li, X., 2021. Cenozoic evolution of the Qaidam basin and implications for the growth of the northern Tibetan plateau: a review. Earth. Sci. Rev. 220, 103730. https://doi.org/10.1016/j.earscirev.2021.103730.

Clark, M.K., Royden, L.H., 2000. Topographic ooze: building the eastern margin of Tibet by lower crustal flow. Geology. 28, 703–706. https://doi.org/10.1130/0091-7613(2000)28%253C703:TOBTEM%253E2.0.CO;2.

Dai, L.-Q., Zheng, F., Zhao, Z.-F., Zheng, Y.-F., 2018. Geochemical insights into the lithology of mantle sources for cenozoic alkali basalts in West Qinling, China. Lithos. 86–98. https://doi.org/10.1016/j.lithos.2017.12.013, 302–303.

Deng, Y., Li, J., Song, X., Zhu, L., 2018. Joint inversion for lithospheric structures: implications for the growth and deformation in northeastern Tibetan plateau. Geophys. Res. Lett. 45, 3951–3958. https://doi.org/10.1029/2018GL077486.

Di Giacomo, D., Engdahl, E.R., Storchak, D.A., 2018. The ISC-GEM Earthquake Catalogue (1904–2014): status after the Extension Project. Earth. Syst. Sci. Data 10, 1877–1899. https://doi.org/10.5194/essd-10-1877-2018.

Ding, L., Kapp, P., Cai, F., Garzione, C.N., Xiong, Z., Wang, H., Wang, C., 2022. Timing and mechanisms of Tibetan Plateau uplift. Nat. Rev. Earth. Environ. 3, 652–667. https://doi.org/10.1038/s43017-022-00318-4.

Dong, Y., Santosh, M., 2016. Tectonic architecture and multiple orogeny of the Qinling Orogenic Belt, Central China. Gondwana Res. 29, 1–40. https://doi.org/10.1016/j.gr.2015.06.009.

Dong, Y., Sun, S., Santosh, M., Hui, B., Sun, J., Zhang, F., Cheng, B., Yang, Z., Shi, X., He, D., Yang, L., Cheng, C., Liu, X., Zhou, X., Wang, W., Qi, N., 2022. Cross orogenic belts in Central China: implications for the tectonic and paleogeographic evolution of the East Asian continental collage. Gondwana Res. 109, 18–88. https://doi.org/10.1016/j.gr.2022.04.012.

Dougherty, S.L., Jiang, C., Clayton, R.W., Schmandt, B., Hansen, S.M., 2020. Seismic evidence for a fossil slab origin for the Isabella anomaly. Geophys. J. Int. 224, 1188–1196. https://doi.org/10.1093/gji/ggaa472.

England, P., Houseman, G., 1986. Finite strain calculations of continental deformation: 2. Comparison with the India-Asia Collision Zone. J. Geophys. Res. 91, 3664–3676. https://doi.org/10.1029/JB091iB03p03664.

Feng, J., Yao, H., Chen, L., Wang, W., 2022. Massive lithospheric delamination in southeastern Tibet facilitating continental extrusion. Natl. Sci. Rev. 9. https://doi.org/10.1093/nsr/nwab174 nwab174.

Guo, Z., Li, S., Yu, Y., Chen, Y.J., Yang, Y., Xu, B., Liang, X., 2022. Eastward asthenospheric flow from NE Tibet inferred by joint inversion of teleseismic body and surface waves: insight into widespread continental deformation in eastern China. JGR Solid Earth 127. https://doi.org/10.1029/2022JB024410 e2022JB024410.

Hu, X., Garzanti, E., Wang, J., Huang, W., An, W., Webb, A., 2016. The timing of India-Asia collision onset – Facts, theories, controversies. Earth. Sci. Rev. 160, 264–299. https://doi.org/10.1016/j.earscirev.2016.07.014.

Huang, H., Shen, X., Lv, J., Zhang, Y., 2022. Dynamic model of the upper mantle beneath the northeastern Tibetan Plateau - constraints from the 410 km and 660 km discontinuities. Gondwana Res. 106, 224–236. https://doi.org/10.1016/j.gr.2021.12.013.

Huang, Z., Xu, M., Wang, L., Mi, N., Yu, D., Li, H., 2008. Shear wave splitting in the southern margin of the Ordos Block, north China. Geophys. Res. Lett. 35. https://doi.org/10.1029/2008GL035188, 2008GL035188.

Kennett, B.L.N., Engdahl, E.R., 1991. Traveltimes for global earthquake location and phase identification. Geophys. J. Int. 105, 429–465. https://doi.org/10.1111/j.1365-246X.1991.tb06724.x.

Kind, R., Yuan, X., Saul, J., Nelson, D., Sobolev, S.V., Mechie, J., Zhao, W., Kosarev, G., Ni, J., Achauer, U., Jiang, M., 2002. Seismic images of crust and upper mantle beneath Tibet: evidence for Eurasian plate subduction. Science (1979) 298, 1219–1221. https://doi.org/10.1126/science.1078115.

Kumar, A., Mitra, S., Suresh, G., 2015. Seismotectonics of the eastern Himalayan and indo-burman plate boundary systems. Tectonics. 34, 2279–2295. https://doi.org/10.1002/2015TC003979.

Li, B., Zhang, L., Ye, G., Jin, S., Wei, W., Xie, C., Chen, X., 2020. Upper mantle thermal structure beneath the eastern margin of the Tibetan Plateau inferred from electrical structure model. Chin. J. Geophys. 63, 1043–1055. https://doi.org/10.6038/cjg2020N0234.

Li, C., Liu, Z., Wang, S., Xu, Z., Chen, S., You, X., Wang, B., 2022. Prediction of major source rocks distribution in the transition from depressed to rifted basin using seismic and geological data: the Guyang to Linhe formations in the Linhe Depression, Hetao Basin, China. . J. Petrol. Sci. Engineering 214, 110472. https://doi.org/10.1016/j.petrol.2022.110472.

Li, Y., Pan, J., Wu, Q., Ding, Z., 2017. Lithospheric structure beneath the northeastern Tibetan Plateau and the western Sino-Korea Craton revealed by Rayleigh wave tomography. Geophys. J. Int. 210, 570–584. https://doi.org/10.1093/gji/ggx181.

Liu, L., Gao, S.S., Liu, K.H., Griffin, W.L., Li, S., Tong, S., Ning, J., 2022. Mantle dynamics of the North China Craton: new insights from mantle transition zone imaging constrained by *P* -to- *S* receiver functions. Geophys. J. Int. 231, 629–637. https://doi.org/10.1093/gji/ggac210.

Liu, S., Yang, Y., Deng, B., Zhong, Y., Wen, L., Sun, W., Li, Z., Jansa, L., Li, J., Song, J., Zhang, X., Peng, H., 2021. Tectonic evolution of the Sichuan Basin. Earth. Sci. Rev. 213, 103470. https://doi.org/10.1016/j.earscirev.2020.103470.

Lou, X., Van Der Lee, S., Lloyd, S., 2013. AIMBAT: a Python/matplotlib tool for measuring teleseismic arrival times. Seismol. Res. Lett. 84, 85–93. https://doi.org/10.1785/0220120033.

Mo, X., Zhao, Z., Deng, J., Flower, M., Yu, X., Luo, Z., Li, Y., Zhou, S., Dong, G., Zhu, D., Wang, L., 2006. Petrology and Geochemistry of Postcollisional Volcanic Rocks from the Tibetan plateau: Implications for Lithosphere Heterogeneity and Collision-Induced Asthenospheric Mantle flow, in: Postcollisional Tectonics and Magmatism in the Mediterranean Region and Asia. Geological Society of America. https://doi.org/10.1130/2006.2409(24).

Paige, C.C., Saunders, M.A., 1982. LSQR: an algorithm for sparse linear equations and sparse least squares. ACM. Trans. Math. Softw. 8, 43–71. https://doi.org/10.1145/355984.355989.

Peng, L., Liu, Lijun, Liu, Liang, 2022. The fate of delaminated cratonic lithosphere. Earth. Planet. Sci. Lett. 594, 117740. https://doi.org/10.1016/j.epsl.2022.117740.
Portner, D.E., Delph, J.R., Biryol, C.B., Beck, S.L., Zandt, G., Özacar, A.A., Sandvol, E., Türkelli, N., 2018. Subduction termination through progressive slab deformation across Eastern Mediterranean subduction zones from updated P-wave tomography beneath Anatolia. Geosphere 14, 907–925. https://doi.org/10.1130/GES01617.1.
Ren, P., Guo, Z., Liu, Y., Luo, B., Wu, X., 2024. Seismic evidence of basin development in NE Tibetan Plateau in response to deep crustal dynamics from joint inversion of rayleigh wave ellipticity and phase velocity. Geophys. Res. Lett. 51. https://doi.org/10.1029/2024GL108589 e2024GL108589.
Schellart, W.P., Chen, Z., Strak, V., Duarte, J.C., Rosas, F.M., 2019. Pacific subduction control on Asian continental deformation including Tibetan extension and eastward extrusion tectonics. Nat. Commun. 10, 4480. https://doi.org/10.1038/s41467-019-12337-9.
Schulte-Pelkum, V., Monsalve, G., Sheehan, A.F., Shearer, P., Wu, F., Rajaure, S., 2019. Mantle earthquakes in the Himalayan collision zone. Geology. 47, 815–819. https://doi.org/10.1130/G46378.1.
Shen, X., Yuan, X., Liu, M., 2015. Is the Asian lithosphere underthrusting beneath northeastern Tibetan Plateau? Insights from seismic receiver functions. Earth. Planet. Sci. Lett. 428, 172–180. https://doi.org/10.1016/j.epsl.2015.07.041.
Sippl, C., Schurr, B., Yuan, X., Mechie, J., Schneider, F.M., Gadoev, M., Orunbaev, S., Oimahmadov, I., Haberland, C., Abdybachaev, U., Minaev, V., Negmatullaev, S., Radjabov, N., 2013. Geometry of the Pamir-Hindu Kush intermediate-depth earthquake zone from local seismic data. JGR Solid Earth 118, 1438–1457. https://doi.org/10.1002/jgrb.50128.
Song, S., Niu, Y., Su, L., Xia, X., 2013. Tectonics of the North Qilian orogen, NW China. Gondwana Res. 23, 1378–1401. https://doi.org/10.1016/j.gr.2012.02.004.
Sun, A., Zhao, D., Guo, H., 2021. Cracks and fluids in the Northeast Tibetan crust: new insight into seismotectonics. Phys. Earth Planet. Inter. 311, 106634. https://doi.org/10.1016/j.pepi.2020.106634.
Tang, Y., Yin, A., Xu, X., An, K., Zhang, Y., 2023. Tectonic evolution of the triassic Songpan-Ganzi basin as constrained by a synthesis of multi-proxy provenance data. Basin Res. 35, 28–60. https://doi.org/10.1111/bre.12703.
Tapponnier, P., Zhiqin, X., Roger, F., Meyer, B., Arnaud, N., Wittlinger, G., Jingsui, Y., 2001. Oblique stepwise rise and growth of the Tibet plateau. Science (1979) 294, 1671–1677. https://doi.org/10.1126/science.105978.
Taylor, M., Yin, A., 2009. Active structures of the Himalayan-Tibetan orogen and their relationships to earthquake distribution, contemporary strain field, and cenozoic volcanism. Geosphere 5, 199–214. https://doi.org/10.1130/GES00217.1.
Tian, X., Teng, J., Zhang, H., Zhang, Z., Zhang, Y., Yang, H., Zhang, K., 2011. Structure of crust and upper mantle beneath the Ordos Block and the Yinshan Mountains revealed by receiver function analysis. Phys. Earth Planet. Inter. 184, 186–193. https://doi.org/10.1016/j.pepi.2010.11.007.
VanDecar, J.C., Crosson, R.S., 1990. Determination of teleseismic relative phase arrival times using multi-channel cross-correlation and least squares. Bull. Seismol. Soc. Am. 80, 150–169. https://doi.org/10.1785/BSSA0800010150.
Wang, W., Huang, R., Wu, Y., Liu, K., Zhang, Z., Zhang, Y., Liu, C., Zheng, D., Zhang, P., 2023. Cenozoic clockwise rotation of the northeastern Tibetan Plateau: paleomagnetic evidence from volcanic sequences in the West Qinling Mountain. Glob. Planet. Change 224, 104097. https://doi.org/10.1016/j.gloplacha.2023.104097.
Wang, W., Wu, J., Fang, L., Lai, G., Cai, Y., 2017a. Sedimentary and crustal thicknesses and Poisson's ratios for the NE Tibetan Plateau and its adjacent regions based on dense seismic arrays. Earth. Planet. Sci. Lett. 462, 76–85. https://doi.org/10.1016/j.epsl.2016.12.040.
Wang, X., Li, Y., Ding, Z., Zhu, L., Wang, C., Bao, X., Wu, Y., 2017b. Three-dimensional lithospheric *S* wave velocity model of the NE Tibetan Plateau and western North China Craton. JGR Solid Earth 122, 6703–6720. https://doi.org/10.1002/2017JB014203.
Wang, X., Wu, H., Wang, H., Wu, B., Huang, Z., 2022. Rayleigh wave tomography of central and southern Mongolia. Tectonophysics. 836, 229426. https://doi.org/10.1016/j.tecto.2022.229426.
Wessel, P., Luis, J.F., Uieda, L., Scharroo, R., Wobbe, F., Smith, W.H.F., Tian, D., 2019. The generic mapping tools version 6. Geochem. Geophys. Geosyst. 20, 5556–5564. https://doi.org/10.1029/2019GC008515.
Xia, B., Artemieva, I.M., Thybo, H., Klemperer, S.L., 2023. Strong variability in the thermal structure of Tibetan lithosphere. JGR Solid Earth 128. https://doi.org/10.1029/2022JB026213 e2022JB026213.
Xu, Q., Pei, S., Yuan, X., Zhao, J., Liu, H., Tu, H., Chen, S., 2019. Seismic evidence for lateral asthenospheric flow beneath the northeastern Tibetan plateau derived from *S* receiver functions. Geochem. Geophys. Geosyst. 20, 883–894. https://doi.org/10.1029/2018GC007986.
Xu, Z., Li, H., Tian, Y., Wang, Q., Yu, C., Li, G., Ji, S., Faure, M., Chevalier, M.-L., 2024. Formation, reactivation and exhumation of the extruded basement wedge in the southern Longmen Shan, eastern Tibetan plateau. JGS 181. https://doi.org/10.1144/jgs2023-088 jgs2023-088.
Yin, A., Harrison, T.M., 2000. Geologic evolution of the himalayan-tibetan orogen. Annu Rev. Earth. Planet. Sci. 28, 211–280. https://doi.org/10.1146/annurev.earth.28.1.211.
Yin, A., Nie, S., 1993. An indentation model for the North and South China collision and the development of the Tan-Lu and Honam Fault Systems, eastern Asia. Tectonics 12, 801–813. https://doi.org/10.1029/93TC00313.
Yu, J., Zheng, D., Wang, W., Pang, J., Li, C., Wang, Y., Hao, Y., Zhang, H., Zhang, P., 2023. Cenozoic tectonic development in the northeastern Tibetan Plateau: evidence from thermochronological and sedimentological records. Glob. Planet. Change 224, 104098. https://doi.org/10.1016/j.gloplacha.2023.104098.
Yu, S., Peng, Y., Zhang, J., Li, S., Santosh, M., Li, Y., Liu, Y., Gao, X., Ji, W., Lv, P., Li, C., Jiang, X., Qi, L., Xie, W., Xu, L., 2021a. Tectono-thermal evolution of the Qilian orogenic system: tracing the subduction, accretion and closure of the Proto-Tethys Ocean. Earth. Sci. Rev. 215, 103547. https://doi.org/10.1016/j.earscirev.2021.103547.
Yu, Y., Chen, Y.J., 2016. Seismic anisotropy beneath the southern Ordos block and the Qinling-Dabie orogen, China: eastward Tibetan asthenospheric flow around the southern Ordos. Earth. Planet. Sci. Lett. 455, 1–6. https://doi.org/10.1016/j.epsl.2016.08.026.
Yu, Y., Chen, Y.J., Feng, Y., An, M., Liang, X., Guo, Z., Qu, W., Li, S., Dong, S., 2021b. Asthenospheric flow channel from northeastern Tibet imaged by seismic tomography between Ordos Block and Yangtze Craton. Geophys. Res. Lett. 48. https://doi.org/10.1029/2021GL093561 e2021GL093561.
Zhang, C., Guo, Z., Chen, Y.J., 2020. Lithospheric thickening controls the ongoing growth of northeastern Tibetan plateau: evidence from *P* and *S* receiver functions. Geophys. Res. Lett. 47. https://doi.org/10.1029/2020GL088972 e2020GL088972.
Zhang, F., Wu, Q., Ding, Z., 2018a. A P-wave velocity study beneath the eastern region of Tibetan Plateau and its implication for plateau growth. Chin. Sci. Bull. 63, 1949–1961. https://doi.org/10.1360/N972018-00337.
Zhang, F., Wu, Q., Li, Y., Zhang, R., Sun, L., Pan, J., Ding, Z., 2018b. Seismic tomography of eastern Tibet: implications for the Tibetan plateau growth. Tectonics. 37, 2833–2847. https://doi.org/10.1029/2018TC004977.
Zhang, G., Shen, W., Fu, G., Li, Z., Zhu, Y., Wang, Y., 2021. Moho changes beneath the northeastern Tibetan plateau revealed by multiple geodetic datasets. JGR Solid Earth 126. https://doi.org/10.1029/2021JB022060 e2021JB022060.
Zhang, Y., Liao, C., Shi, W., Zhang, T., Guo, F., 2007. Jurassic deformation in and around the Ordos Basin, North China. Earth Sci. Front. 14, 182–196. https://doi.org/10.1016/S1872-5791(07)60016-5.
Zhang, Y.Q., Mercier, J.L., Vergély, P., 1998. Extension in the graben systems around the Ordos (China), and its contribution to the extrusion tectonics of south China with respect to Gobi-Mongolia. Tectonophysics. 285, 41–75. https://doi.org/10.1016/S0040-1951(97)00170-4.
Zhao, D., Hasegawa, A., Horiuchi, S., 1992. Tomographic imaging of *P* and *S* wave velocity structure beneath northeastern Japan. J. Geophys. Res. 97, 19909–19928. https://doi.org/10.1029/92JB00603.
Zhao, D., Hasegawa, A., Kanamori, H., 1994. Deep structure of Japan subduction zone as derived from local, regional, and teleseismic events. J. Geophys. Res. 99, 22313–22329. https://doi.org/10.1029/94JB01149.
Zhu, R., Chen, L., Wu, F., Liu, J., 2011. Timing, scale and mechanism of the destruction of the North China Craton. Sci. China Earth. Sci. 54, 789–797. https://doi.org/10.1007/s11430-011-4203-4.
Zuza, A.V., Cheng, X., Yin, A., 2016. Testing models of Tibetan Plateau formation with cenozoic shortening estimates across the Qilian Shan–Nan Shan thrust belt. Geosphere 12, 501–532. https://doi.org/10.1130/GES01254.1.